

An 18 – 25 GHz spectroscopic survey of dense cores in the Chamaeleon I molecular cloud

Dariusz C. Lis¹, William D. Langer¹, Jorge L. Pineda¹, Kahaan Gandhi^{2,1}, Karen Willacy¹, Paul F. Goldsmith¹, Susanna Widicus Weaver^{3,4}, Liton Majumdar^{5,6}, Youngmin Seo⁷, Shinji Horiuchi⁸, Cheikh Bop^{9,10}, and François Lique⁹

¹ Jet Propulsion Laboratory, California Institute of Technology, 4800 Oak Drove Drive, Pasadena, CA 91109, USA

² Haverford College, 370 Lancaster Avenue, Haverford, PA 19041, USA

³ Department of Astronomy, University of Wisconsin-Madison, 475 N Charter St, Madison, WI 53706, USA

⁴ Department of Chemistry, University of Wisconsin-Madison, 1101 University Ave, Madison, WI 53706, USA

⁵ Exoplanets and Planetary Formation Group, School of Earth and Planetary Sciences, National Institute of Science Education and Research, Jatni 752050, Odisha, India

⁶ Homi Bhabha National Institute, Training School Complex, Anushaktinagar, Mumbai 400094, India

⁷ Aerospace Corporation, 4745 Lee Road, Chantilly, VA 20151, USA

⁸ CSIRO Space & Astronomy/NASA Canberra Deep Space Communication Complex, PO Box 1035, Tuggeranng ACT 2901, Australia

⁹ Univ. Rennes, CNRS, IPR (Institut de Physique de Rennes) – UMR 6251, 35000 Rennes, France

¹⁰ Nantes Université, CNRS, CEISAM, UMR 6230, F-44000 Nantes, France

Received 24 January 2025; accepted 3 Mar 2025

ABSTRACT

The presence of over 300 molecules in the interstellar medium, the majority of them organic compounds, raises the question of the extent to which protostellar chemistry is responsible for organic molecules in solar system bodies (e.g., comets, asteroids, planets). The majority of systematic surveys for organic molecules in cold cores have focused on the TMC-1 core in the Taurus complex, along with lesser surveys of other protostellar cores in the northern hemisphere facilitated by the presence of several telescopes available for surveys below 45 GHz, where most organic molecules have relatively strong emission under conditions in cold cores. A few southern hemisphere sources have been surveyed at wavelengths between 7 and 1 mm. Here we extend the survey for organics in the southern hemisphere to 1.3 cm by observing two cores in the Chamaeleon complex using NASA's Deep Space Network 70-m antenna in Canberra, Australia, over the frequency range of 18 to 25 GHz. In the Chamaeleon complex we surveyed the class 0 protostar Cha-MMS1 and the prestellar core Cha-C2, which represent two stages in the evolution of dense cores. We detect several molecules including HC₃N, HC₅N, C₄H, CCS, C₃S, NH₃, and c-C₃H₂. A longer cyanopolyne, HC₇N, is detected with high confidence via spectral stacking analysis. While molecular column densities in the two Chamaeleon cores are typically an order of magnitude lower compared to the cyanopolyne peak in TMC-1, the molecular abundance ratios are in general agreement with the TMC-1 values. The two exceptions are c-C₃H₂, which is enhanced by a factor of ~25 with respect to cyanopolyynes in the Chamaeleon cores, and ammonia, which is enhanced by a factor of ~125. The deuterated species c-C₃HD is detected in both cores, with a high D/H ratio of ~0.23 in c-C₃H₂. A rare isotopologue of ammonia, ¹⁵NH₃, is also detected in Cha-MMS1 suggesting a high ¹⁴N/¹⁵N ratio of ~690 in ammonia. However, this ratio may be artificially enhanced due to the high optical depth of the ¹⁴NH₃ (1,1) line, which increases the effective source size. We use the detections of ammonia, cyanopolyynes, and far-infrared dust continuum to characterize the density and temperature in the Chamaeleon cores and calculate the molecular column densities and their relative ratios. The ring molecule benzonitrile, a tracer for the non-polar molecule benzene, is not detected in either Chamaeleon core. The 3σ upper limits for the benzonitrile column density achieved are a factor of 2 higher than the value derived for TMC-1 and the corresponding upper limits for the relative abundance of benzonitrile with respect to HC₅N are a factor of 3 higher than the TMC-1 value.

Key words. Astrochemistry – ISM: abundances – ISM: clouds – ISM: lines and bands – ISM: molecules

1. Introduction

An extrasolar origin has been proposed as a possible source of complex organic molecules and water detected in primitive solar system bodies (e.g., Hanni et al. 2022). Many of the same molecules have been detected in the interstellar medium, in particular in protostellar cores and protoplanetary disks. However, the chemical pathways for their production via gas phase and grain catalysis from atomic and molecular species are not well established, nor are the mechanisms for their incorporation into solar bodies such as comets and planets. To answer these ques-

tions, searches have been conducted to detect molecules in both the gas phase and in ices in a variety of interstellar sources. To date, astronomical observations have detected over 320 individual molecular species in the gas phase in interstellar, protostellar, and circumstellar environments (McGuire, 2022).¹ Furthermore, the majority of these detections are of organic molecules, made of carbon bonded with other elements or other carbon atoms. Most of these discoveries have been detections enabled by radio astronomy of spectral signatures of molecules rang-

¹ See also <http://astrochymist.org>

ing in size from two (e.g., OH and CO) to thirteen atoms in the long chain HC₁₁N and recently detected ring molecule benzonitrile, C₆H₅CN (McGuire et al., 2018), and even larger polycyclic aromatic hydrocarbons C₁₀H₇CN (McGuire et al., 2021), C₁₂H₈ (Cernicharo et al., 2024), or C₁₆H₉CN (Wenzel et al., 2024).

Systematic searches for species in a broad range of sources is needed so that a complete picture of their abundances can be developed in order to determine the chemical pathways forming complex organic molecules. In the northern hemisphere the "Astrochemical Surveys at IRAM" (ASAI) carried out an unbiased spectral survey between 80 and 272 GHz of 10 sources spanning a range of evolutionary states, including the starless core TMC-1 in the Taurus Molecular Cloud (Lefloch et al., 2018). TMC-1 is one of the richest interstellar sources of organic molecules and it has also been the target of dedicated radio observations of emission spectra at longer wavelengths. The two current systematic studies of TMC-1 at longer wavelengths are QUIJOTE, Q-Band Ultrasensitive Inspection Journey to the Obscure TMC-1 Environment, using the Yebes telescope (Cernicharo et al., 2021) and GOTHAM, GBT Observations of TMC-1: Hunting Aromatic Molecules, at the Green Bank Telescope (McGuire et al., 2018). Most of the other sources that have been systematically surveyed are highly evolved regions of massive star formation, such as Sgr B2 and Orion, or evolved stars such as IRC+10216. However, broad spectral surveys of cold protostellar cores, even those residing in regions of massive star formation, such as is thought to be the environment in which the solar system formed, are much less explored. The excitation conditions at low temperatures and high densities in these cold cores favor observational surveys at wavelengths ≥ 3 mm, and for the heavier organics ≥ 7 mm.

In the southern hemisphere far fewer sources have been studied systematically at long wavelengths. The Australia Telescope Compact Array has conducted a Q-band survey of Sagittarius B2 and detected over 53 molecular species (Corby et al., 2015). However, Sgr B2 is an atypical Galactic source, and so its chemistry may be more characteristic of energetic massive star forming cores rather than the pathway to solar-type planet forming disks. In the southern hemisphere the best studied low-mass protostar at long wavelengths is Chameleon MMS1 which was observed by Kontinen et al. (2000) at 3 mm wavelength with the Swedish-ESO Submillimeter Telescope (SEST) and by Cordiner et al. (2012) at 7 mm wavelength with the ATNF Mopra 22m telescope. The Chameleon complex is also a target of the JWST "Ice Age" ERS program (McClure et al., 2023) ultimately making it possible to compare gas phase and ice phase chemistry.

Located at a distance of 190 pc (Galli et al., 2021), Chamaeleon I is one of the closest low-mass star forming regions in the southern hemisphere (Belloche et al. 2011 and references therein). Embedded within the Chamaeleon I ridge traced by millimeter dust continuum emission are a known prestellar core, a Class 0 protostar, a binary protostellar system Ced 110 IRS4 (Rocha et al., 2025), and an edge-on Class II protoplanetary disk HH 48 NE (Sturm et al., 2024). To cover a range of physical environments most relevant for the complex organic molecule (COM) chemistry, we selected the Class 0 protostar (Cha-MMS1) and the prestellar core (Cha-C2) as targets of our observations.

In this paper we extend the survey of Chameleon to radio K-band using NASA's Deep Space Network (DSN) 70-m antenna in Canberra, Australia (DSS-43) covering the 18 to 25 GHz frequency range. The two Chamaeleon sources studied here have different ages, with the class 0 protostar Cha-MMS1 being more evolved than the prestellar core Cha-C2. Moreover, being surrounded by a group of YSO's, the two cores are located in a

different environment than the best studied starless core, TMC-1. The observations thus provide interesting insights into the effects of environment and age on the dense core chemistry. We use multi-wavelength *Herschel* observations of the dust continuum emission and multiple transitions of ammonia, HC₃N, and HC₅N to derive the kinetic temperatures and densities of the two cores.

In Section 2 we discuss the DSS-43 observations and in Section 3 we derive the properties of the cores and molecular column densities. In Section 4 we use a Markov Chain Monte Carlo (MCMC) analysis to identify features in the spectral scans that are too weak to identify from individual spectral lines. In Section 5 we discuss the differences between the Chamaeleon sources and TMC-1. In Section 6 we summarize our results and describe the next steps needed to trace the evolution of prebiotic compounds in protostellar cores.

2. Deep Space Network observations

The Deep Space Network radio telescopes had a nearly decade-long history of contributions to the search for organic molecules in the northern hemisphere and study of their formation environment beginning in the early 1990s (Langer et al., 1995; Velusamy et al., 1995; Kuiper et al., 1996; Langer et al., 1997, 1998; Peng et al., 1998; Dickens et al., 2001). The DSN technical capabilities for astrochemistry research have improved significantly in recent years with the installation of a new cryogenic dual-horn dual-polarization 17–27 GHz receiver at the Deep Space Station 43 (DSS-43) in Canberra, Australia (Kuiper et al., 2019), with its broadband digital spectrometer (Virkler et al., 2020). The wide instantaneous bandwidth allows observations of multiple transitions of heavy species which can be used to characterize the density and temperature of the gas using radiative transfer models, and dynamical information from the line width and velocity at the line peak. The spectrometer provides sufficiently high spectral resolution to resolve molecular line shapes even in the coldest regions (~ 10 K) of protostellar cores.

Several observing runs of the Chamaeleon I cloud using the DSN 70-m antenna at Canberra were carried out in February – September, 2022. Figure 1 shows the overall morphology of the region as traced by 350 μ m dust emission observed with the SPIRE instrument on *Herschel*. The black circles show the two DSS-43 pointings, centered on the class 0 protostar MMS1 and the prestellar core C2. The J2000 source coordinates for Cha-MMS1 are $\alpha = 11^{\text{h}}06^{\text{m}}33.13^{\text{s}}$, $\delta = -77^{\circ}23'35.1''$ and for Cha-C2 $\alpha = 11^{\text{h}}06^{\text{m}}15.51^{\text{s}}$, $\delta = -77^{\circ}24'04.9''$. All observations were carried out in a position-switching mode, using a reference position 5' N-W of Cha-MMS1, in a direction perpendicular to the extent of the dust ridge (at $11^{\text{h}}05^{\text{m}}30.00^{\text{s}}$, $-77^{\circ}21'00.0''$; white circle in the upper-right corner of Fig. 1). Circle sizes correspond to the FWHM beam size of the Canberra telescope at 22 GHz, 45''. The filled black circle in the lower-left corner shows the SPIRE 350 μ m FWHM beam size of 25.2''.

The 350 μ m continuum emission in Chamaeleon I is extended on scales comparable to the DSS-43 beam size (see 50% white dotted contour in Fig. 1). Belloche et al. (2011) derive FWHM source sizes of $55'' \times 49''$ and $98'' \times 46''$ for Cha-MMS1 and Cha-C2, respectively, based on observations of 870 μ m dust continuum emission using the APEX telescope. We thus assume average source sizes of 52 and 67'' in the column density calculations.

The DSN Canberra K-band digital spectrometer processes sixteen 1-GHz wide bands, split into 8 separate bands from 18 to 26 GHz for each polarization (Virkler et al., 2020). Each band

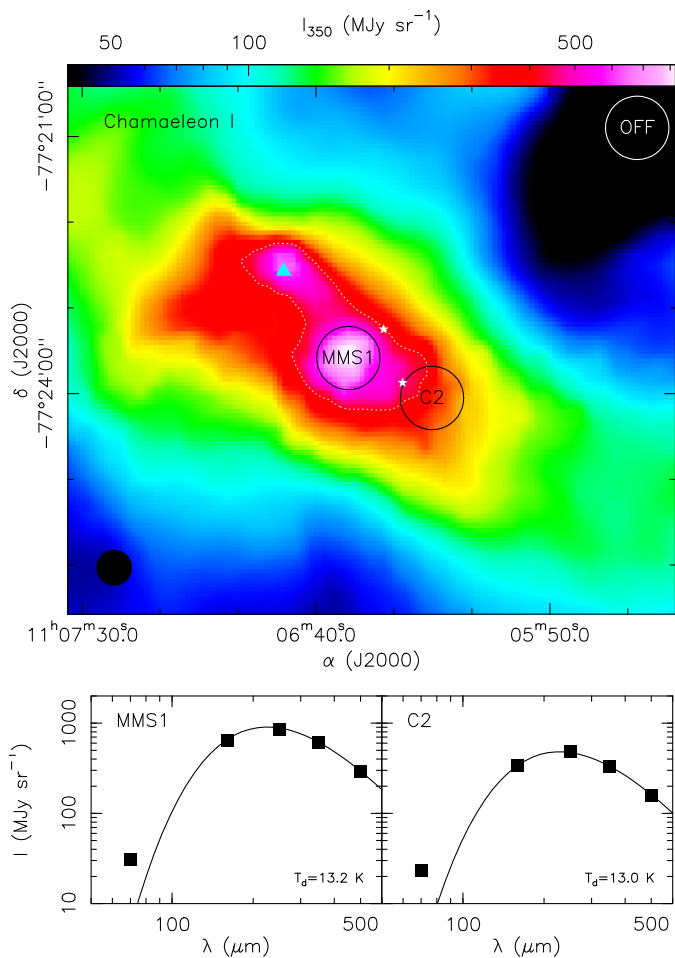


Fig. 1. *Herschel*/SPIRE image of 350 μm dust continuum emission toward the central part of the Chamaeleon I cloud. The dotted contour outlines the extent of the dust emission at 50% of the peak. Black circles mark the Cha-MMS1 and Cha-C2 pointings and the white circle indicates the reference position used for the DSN observations. The size of the two circles corresponds to the FWHM beam size of the Canberra telescope (45"). The black circle in the lower-left corner shows the FWHM size of the SPIRE beam (25.2"). White asterisks mark locations of NIR38 and J110621228, two background stars with ice spectra studied by McClure et al. (2023), and the cyan triangle marks the location of the binary protostar Ced 110 IRS4 (Rocha et al. 2025). The lower panels show the dust continuum SED in the Canberra beam, based on PACS and SPIRE observations. The black curves are modified blackbody fits to the SPIRE and PACS 160 μm surface brightness, as described in the text. Typical flux calibration uncertainties are 5%.

consists of 32,768 channels with a 30.5 kHz resolution, corresponding to a velocity resolution of 0.35 – 0.49 km s^{-1} , depending on the frequency. A typical FWHM line width in Cha-MMS1 is 0.6 – 0.9 km s^{-1} , depending on the species. All lines are thus spectrally resolved. A typical system temperature at the elevation of the source was 77 K. The total on-source integration time was about 14 hours per source. For the seven lowest-frequency bands, 2 instrumental polarizations were observed, doubling the effective observing time. At frequencies above 25 GHz, only one instrumental polarization was available. The resulting spectra thus have higher noise and are not included in the analysis.

The raw data from the spectrometer were processed into calibrated ON-OFF spectra using the standard DSS-43 data reduction pipeline. The system temperature was continuously moni-

tored using a power meter, scaling with a factor derived using a noise diode and an ambient load before the observation; it is used in the standard ON-OFF calibration to obtain spectra in the antenna temperature units, T_A^* . We refer the reader to Kuiper et al. (2019) for details on the absolute system and receiver temperature calibration. A relative gain correction was applied to the data to account for antenna deformations as a function of elevation. The gain dependence on elevation was determined using measurements of a flux calibrator at different elevations, showing a peak at about 45° elevation. Kuiper et al. (2019) fitted a third order polynomial to the data, but we used a second order fit, as discussed in the ATNF Tidbinbilla 70-m Radio Telescope Guide², which provides more accurate values for observations taken at high elevations.

The beam efficiency was not measured directly during our observations. To convert the observed spectra to the main beam brightness temperature units, we use the main beam efficiency of $\eta_{mb} = 50\%$ (Pineda et al., 2019) rather than the measured DSN aperture efficiency of $\eta_A = 35.5\%$. This choice is justified given the expected extent of the molecular emission. Moreover, the absolute intensity calibration is not critical, as opacity effects are small or moderate for all detected lines except for ammonia, and we use only the relative abundance ratios among the molecules rather than absolute abundances with respect to H_2 in the comparison with TMC-1.

Subsequent data reduction was carried out using the IRAM CLASS data reduction software³. The data reduction included blanking of noisy channels near the band edges and removing 3rd order polynomial baselines from individual scans, fitted across the full frequency range of each band. The resulting baseline-removed spectra were then averaged with $1/\sigma^2$ weighting to produce the final spectra used in the analysis.

The resulting full-band spectra of Cha-MMS1 and C2 (in antenna temperature T_{mb}^* units) are shown in Figure 2, with the strongest molecular lines labeled. The noise level is not uniform, and often increases significantly toward the band edges. In addition, some noise spikes (“spurs”) are present in the spectra. Channels with excess noise near band edges and narrow spurious signals have been blanked, resulting in some gaps in the frequency coverage. The origin of these artifacts was not investigated, as they do not affect any of the spectral lines discussed below.

Since in some cases the rms can vary significantly across the subband, spectra of all lines identified in the broadband survey were subsequently re-reduced by computing the local noise in the immediate vicinity of each line and using this value in the weighted average.

3. Results

In this section we discuss the physical conditions in the Chamaeleon cores based on prior observations. We then derive LTE, and for some species non-LTE, molecular column densities and molecular abundance ratios and compare them with those toward the cyanopolyne peak in TMC-1 (Gratier et al., 2016). TMC-1, a target of the QUIJOTE and GOTHAM surveys (Cernicharo et al., 2021; McGuire et al., 2018), is the best studied dense core and a reference source for astrochemical studies. Observations of other cores, such as those studied here, will help

² https://www.atnf.csiro.au/resources/observing/observers/tidbinbilla/tid_obs_guide/

³ <https://www.iram.fr/IRAMFR/GILDAS/>

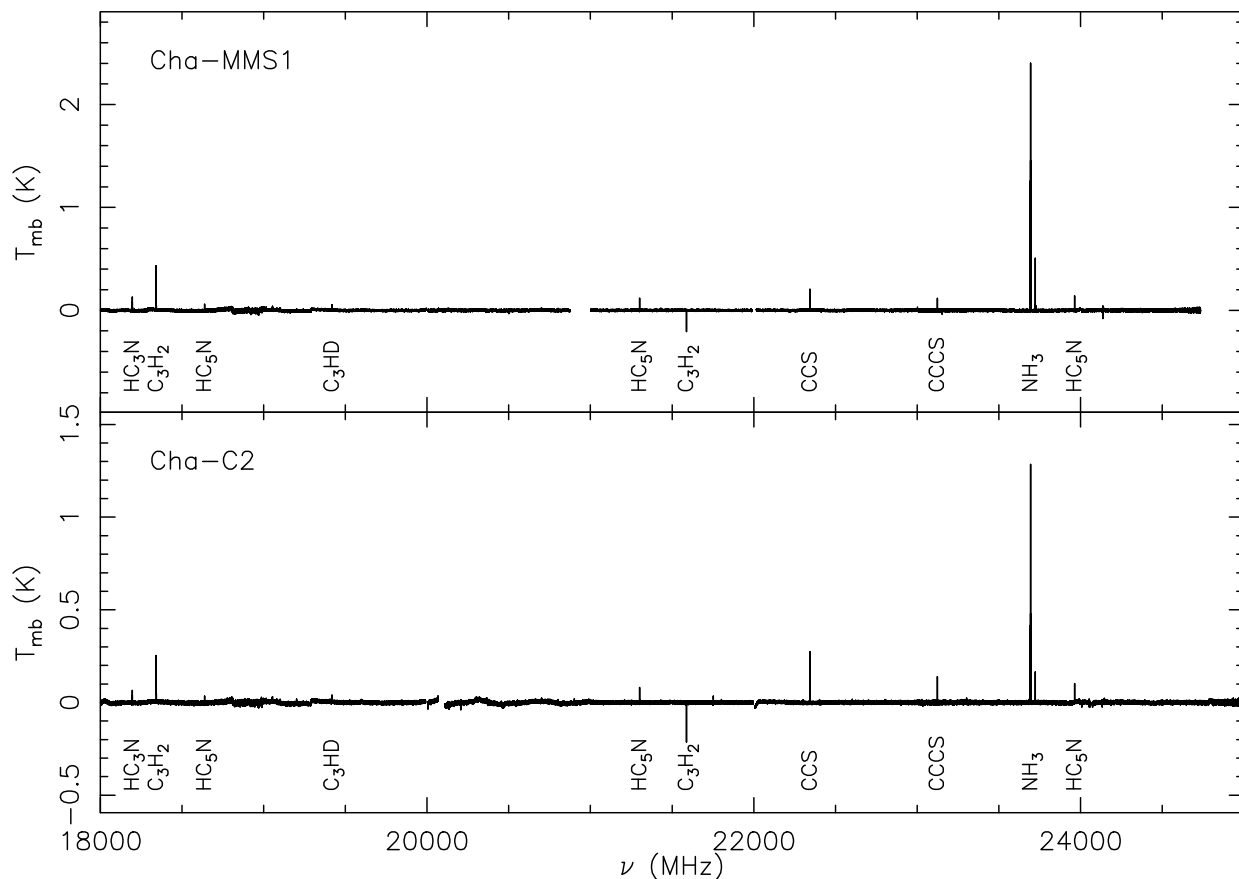


Fig. 2. DSN spectra of Cha MMS1 and Cha C2 (upper and lower panel, respectively) corrected for the main beam efficiency. Channels with excess noise near subband edges and spurious signals have been blanked, resulting in some gaps in the frequency coverage. Detected spectral lines are identified (see Tables 1 and 2).

Table 1. Parameters of fits to lines observed in Chamaeleon MMS1.

Transition	ν_o (MHz)	t (hr)	σ (mK)	$\int T_{mb} dv$ (mK kms ⁻¹)	V_{LSR} (kms ⁻¹)	ΔV (kms ⁻¹)
HC ₃ N (2 – 1)	18196.2300	26.7	3.8	338. (10.)	3.96 (0.01)	0.84 (0.01)
c-C ₃ H ₂ (1 ₁₀ – 1 ₀₁)	18343.1430	26.7	3.9	513. (4.0)	3.83 (0.01)	0.84 (0.01)
HC ₅ N (7 – 6)	18638.6164	26.7	4.5	86.7 (4.5)	3.92 (0.03)	0.82 (0.02)
C ₄ H (2 – 1, 5/2 – 3/2, 2 – 1)	19014.7204	26.7	3.8	20.8 (4.5)	4.18 (0.08)	0.81 (0.25)
C ₄ H (2 – 1, 5/2 – 3/2, 3 – 2)	19015.1435	26.7	3.6	26.0 (3.7)	4.15 (0.04)	0.64 (0.29)
C ₄ H (2 – 1, 3/2 – 1/2, 2 – 1)	19054.4762	26.7	3.8	27.5 (6.2)	4.15 (0.09)	0.71 (0.19)
c-C ₃ HD (1 ₁₀ – 1 ₀₁)	19418.7272	26.7	3.3	71.5 (4.5)	4.12 (0.04)	1.44 (0.12)
HC ₅ N (8 – 7)	21301.2614	26.8	3.6	115. (6.3)	4.04 (0.01)	0.77 (0.03)
c-C ₃ H ₂ (2 ₂₀ – 2 ₁₁)	21587.4010	26.8	2.9	-199. (2.7)	4.03 (0.01)	0.79 (0.01)
CCS (1 – 2, 2 – 1)	22344.0308	26.8	3.0	191. (2.6)	3.88 (0.01)	0.74 (0.01)
¹⁵ NH ₃ (1,1)	22624.9295	26.8	3.2	16.8 (3.3)	3.88 (0.11)	1.04 (0.26)
C ₃ S (4 – 3)	23122.9836	14.0	4.8	88.4 (3.9)	4.33 (0.02)	0.73 (0.04)
NH ₃ (1,1)	23694.4955	14.0	3.5	12,690 (47.)	4.33 (0.01)	0.64 (0.01)
HC ₅ N (9 – 8)	23963.9007	14.0	4.3	131. (3.8)	4.30 (0.01)	0.64 (0.40)
NH ₃ (2,2)	23722.6333	14.0	4.5	648. (4.5)	4.31 (0.01)	0.75 (0.01)
NH ₃ (3,3)	23870.1292	14.0	3.8	10.1 (2.2)	4.26 (0.04)	0.38 (0.65)

Note: Entries in the table are: molecular transition, rest frequency, total observing time including the two polarizations, final rms in a single spectrometer channel in the vicinity of the line, integrated line intensity (opacity corrected for the HFS fits; see Sect. 2.5.3 of the CLASS user manual, <https://www.iram.fr/IRAMFR/GILDAS/doc/pdf/class.pdf>), line velocity, and line width,. Integrated line intensities have been corrected for the beam efficiency, but not for the coupling to the source. Values in parenthesis are 1σ fit uncertainties. The opacity of the main NH₃ (1,1) hyperfine component implied by the HFS fit is 7.63 ± 0.05 .

Table 2. Parameters of fits to lines observed in Chamaeleon C2.

Transition	ν_o (MHz)	t (hr)	σ (mK)	$\int T_{mb} dv$ (mK kms ⁻¹)	V_{LSR} (kms ⁻¹)	ΔV (kms ⁻¹)
HC ₃ N (2 – 1)	18196.2300	22.0	3.4	209. (12.)	3.86 (0.01)	0.89 (0.04)
c-C ₃ H ₂ (1 ₁₀ – 1 ₀₁)	18343.1430	22.0	3.2	344. (3.5)	3.82 (0.01)	0.92 (0.01)
HC ₅ N (7 – 6)	18638.6164	22.0	3.9	56.2 (4.0)	3.83 (0.04)	0.82 (0.01)
C ₄ H (2 – 1, 5/2 – 3/2, 2 – 1)	19014.7204	22.0	3.7	15.9 (4.1)	4.23 (0.11)	0.91 (0.24)
C ₄ H (2 – 1, 5/2 – 3/2, 3 – 2)	19015.1435	22.0	3.7	23.0 (4.3)	4.20 (0.10)	1.08 (0.24)
C ₄ H (2 – 1, 3/2 – 1/2, 2 – 1)	19054.4762	22.0	3.7	40.5 (7.8)	3.93 (0.16)	1.60 (0.35)
c-C ₃ HD (1 ₁₀ – 1 ₀₁)	19418.7272	22.0	3.5	48.7 (5.0)	4.11 (0.06)	1.42 (0.21)
HC ₅ N (8 – 7)	21301.2614	22.0	3.4	92.9 (4.7)	3.95 (0.01)	0.79 (0.04)
c-C ₃ H ₂ (2 ₂₀ – 2 ₁₁)	21587.4010	22.0	3.2	-210. (3.0)	4.04 (0.01)	0.88 (0.02)
CCS (1 – 2, 2 – 1)	22344.0308	22.0	2.9	252. (2.7)	3.85 (0.01)	0.81 (0.01)
¹⁵ NH ₃ (1,1)	22624.9295	22.0	3.3	< 11.0 ^c		
C ₃ S (4 – 3)	23122.9836	18.5	3.9	119. (3.4)	4.27 (0.01)	0.78 (0.03)
NH ₃ (1,1)	23694.4955	18.5	3.1	3,751 (29.)	4.22 (0.01)	0.69 (0.01)
HC ₅ N (9 – 8)	23963.9007	18.5	3.3	95.1 (3.0)	4.23 (0.01)	0.73 (0.09)
NH ₃ (2,2)	23722.6333	18.5	3.4	192. (30.)	4.23 (0.01)	0.70 (0.01)
NH ₃ (3,3)	23870.1292	18.5	3.5	< 11.1 ^c		
U22902	22902.037	22.0	3.6	26.9 (3.6)	4.16 (0.06)	0.098 (0.17)

Note: Entries in the table are: molecular transition, rest frequency, total observing time including the two polarizations, final rms in a single spectrometer channel in the vicinity of the line, integrated line intensity (opacity corrected for the HFS fits; see Sect. 2.5.3 of the CLASS user manual, <https://www.iram.fr/IRAMFR/GILDAS/doc/pdf/class.pdf>), line velocity, and line width. Integrated line intensities have been corrected for the beam efficiency, but not for the coupling to the source. Values in parenthesis are 1σ fit uncertainties. ^aOptically thin line. ^bGaussian fit. ^c 3σ upper limit, integrated over 2.5 – 5.5 km s⁻¹ velocity range. An unidentified $\sim 7.5\sigma$ feature is detected at 22.902 GHz, which is not present in the Cha-MMS1 spectrum. The opacity of the main NH₃ (1,1) hyperfine component implied by the HFS fit is 2.85 ± 0.04 .

Table 3. Physical properties of the Chamaeleon MMS1 and C2 cores.

	MMS1	C2
T_d (K)	13.2	13.0
T_g (K)	8.5–10.9	8.5–10.9
N_{H_2} (cm ⁻²)	$4 - 17 \times 10^{22}$	$2.5 - 10 \times 10^{22}$
n_{H_2} (cm ⁻²)	$3 - 14 \times 10^5$	$2 - 8 \times 10^5$

Note: Physical parameters are mean values within the 45'' DSS-43 beam.

determine to what extent the chemistry of TMC-1 is representative of typical dense cores.

Figure 2 shows the radio K-band spectra of the Chamaeleon MMS1 and C2 cores taken with the Canberra DSN telescope. The main individual lines detected, including those of HC₃N, HC₅N, c-C₃H₂, C₄H, CCS, C₃S, NH₃, and the rare isotopologues ¹⁵NH₃ and c-C₃HD, are shown in more detail in Figures 3 and 4. The line parameters derived from Gaussian and hyperfine-structure (HFS) fits are listed in Tables 1 and 2. Below we derive the molecular column densities and relative fractional abundances of the detected molecules, as well as upper limits for selected molecular species.

3.1. Densities and temperatures of the Chamaeleon cores

Calculations of molecular column densities require prior knowledge of the gas temperature (local thermodynamical equilibrium, LTE, calculations), or temperature and density (radiative transfer models, such as the large velocity gradient, LVG, approach).

These physical parameters can be estimated from the existing dust continuum as well as molecular data, given that multiple transitions covering a range of excitation conditions are detected.

The two bottom panels in Figure 1 show dust spectral energy distributions (SEDs) in the DSS-43 beam toward the MMS1 and C2 cores. Modified blackbody fits to the SPIRE and PACS 160 μm surface brightness, $I_\nu = B_\nu(T_d) \times [1 - \exp(-\tau_{350} \times (350\mu\text{m}/\lambda)^\beta)]$, (shown as black curves in the bottom panels of Fig. 1) give average dust temperatures of ~ 13 K and a grain emissivity exponent $\beta = 1.9$ in both cores. We exclude the PACS 70 μm data from the fit, as the emission may be contaminated by a warmer dust component, distributed across the outer layers of the cloud.

The H₂ column densities in the DSS-43 beam can be computed using the formula $N(\text{H}_2) = 2a\rho R_{gd}/3m_{\text{H}} \times \tau_{350}/Q_{350}$ (Lis & Goldsmith, 1990), where $a = 0.1 \mu\text{m}$ is the grain radius, $\rho = 3 \text{ g cm}^{-3}$ is the mean density, $R_{gd} = 100$ is the gas to dust ratio, m_{H} is the hydrogen mass, and Q_{350} is the 350 μm grain emissivity coefficient. Extrapolating the 125 μm grain emissivity of Hildebrand (1983) (7.5×10^{-4}) with a ν^2 frequency dependence gives $Q_{350} = 1 \times 10^{-4}$, corresponding to the grain mass opacity coefficient $\kappa_{350} = 3Q/4/a/\rho/R_{gd} = 0.025 \text{ cm}^2 \text{ g}^{-1}$. The values of Q_{350} and κ_{350} are highly uncertain and values 4 times higher have been suggested for the Orion Molecular Cloud (see the discussion in Lis et al. 1998 and Goldsmith, Bergin, & Lis 1997).

The resulting H₂ column densities toward MMS1 and C2 are thus in the range $N_{\text{H}_2} = 4 - 17 \times 10^{22}$ and $2.5 - 10 \times 10^{22} \text{ cm}^{-2}$, respectively. Assuming a line-of-sight depth equal to $\sim 55''$ (as implied by the 50% contour of the 350 μm emission in Fig. 1) and a distance of 150 pc, the mean H₂ densities in the DSS-43 beam

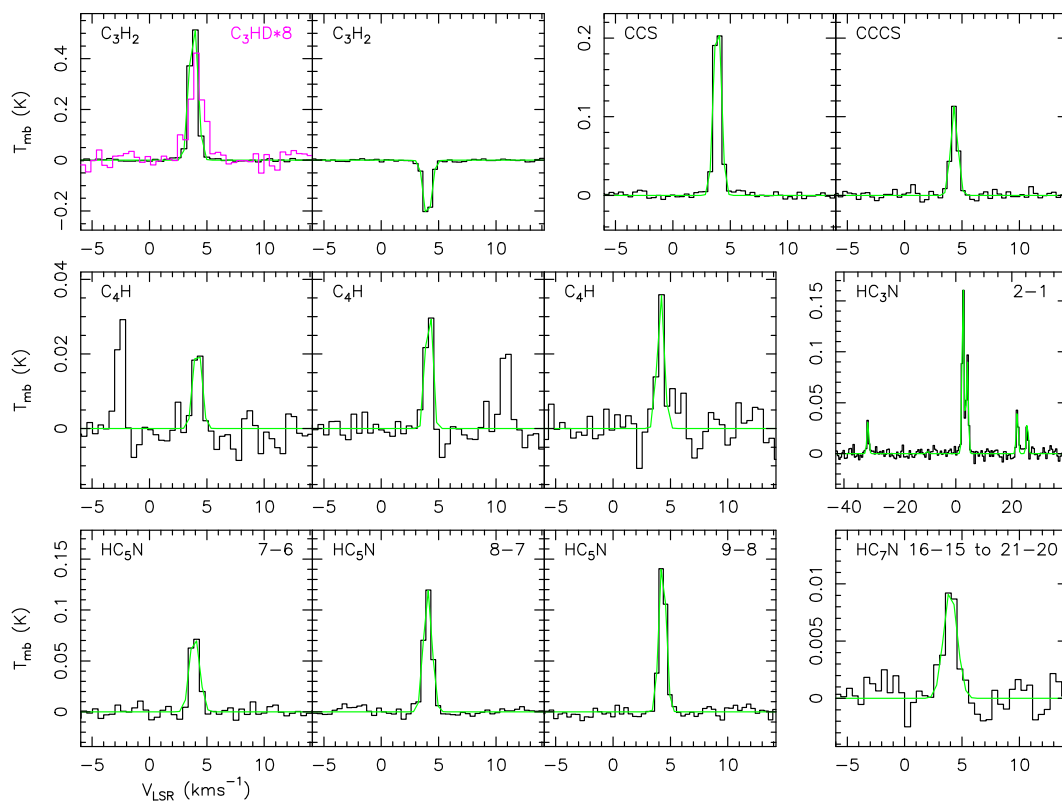


Fig. 3. Spectra of molecular lines other than ammonia detected in Chamaeleon MMS1 (black and magenta histograms) with fits shown in green.

toward MMS1 and C2 are $n_{\text{H}_2} = 3 - 14 \times 10^5$ and $2 - 8 \times 10^5 \text{ cm}^{-3}$, respectively.

A wide range of column and volume densities in Cha MMS1 has been reported in the literature. Kontinen et al. (2000) derived a low H_2 column density of $1.2 - 1.6 \times 10^{22} \text{ cm}^{-2}$ and an average H_2 density of $\sim 7 \times 10^4 \text{ cm}^{-3}$ based on C^{18}O observations using the SEST telescope ($55''$ beam). However, this value depends on the assumed fractional abundance of C^{18}O , which may be lower than the canonical Taurus value (Frerking et al., 1979), if partial freezeout occurs in cold, high density gas.

Tennekes et al. (2006) report a slightly higher H_2 column density range of $1.9 - 4.0 \times 10^{22} \text{ cm}^{-2}$ based on 1.3 mm dust continuum observations. Their spherical Monte Carlo model that fits SEST observations of HCN isotopologues in Cha-MMS1 has densities ranging from $2.3 \times 10^4 \text{ cm}^{-3}$ at the outer $60''$ radius and $1.4 \times 10^6 \text{ cm}^{-3}$ at the center. Cordiner et al. (2012) assume an H_2 density of 10^6 cm^{-3} in the analysis of their ATNF Mopra observations at 32–50 GHz ($96 - 77''$ beam), while Belloche et al. (2011) derive a peak column densities of 9.2 and $2.7 \times 10^{22} \text{ cm}^{-2}$ in a $21''$ beam toward Cha-MMS1 and C2, respectively, and average gas densities in a $50''$ diameter aperture of 9.8×10^5 and $3.9 \times 10^5 \text{ cm}^{-3}$, respectively, based on $870 \mu\text{m}$ dust continuum observations using the APEX telescope.

Observations of HC_3N and HC_5N for which theoretically derived collisional rate coefficients are available can be used to provide an independent estimate of the gas temperature and density. One advantage to this approach is that their emission most likely arises from the same region as other organic molecules. In Appendix A we show that our HC_3N and HC_5N data in conjunction with SEST data of Kontinen et al. (2000) in a similar beam are well reproduced by LVG models with a kinetic temperature of $\sim 8.5 \text{ K}$ and a density $\gtrsim 3 \times 10^5 \text{ cm}^{-3}$. This kinetic temperature is close to the range $7.1 - 7.2 \text{ K}$ derived by Cordiner et al. (2012)

based on Mopra observations of HC_3N and HC_5N in a larger beam.

The average kinetic temperature of the gas within the DSS-43 beam can also be constrained by observations of the inversion lines of ammonia (Appendix B). The rotational temperature of 10.9 K for Cha-MMS1 derived in Appendix B agrees with previous ammonia observations, 12.1 K (Tennekes et al., 2006). These values are higher than the temperature implied by LVG models of HC_3N and HC_5N (Appendix A).

3.2. LTE molecular column densities

There are two possible approaches to converting the observed line intensities to molecular column densities, depending on the availability of collisional rate coefficients. For molecules with calculated rate coefficients we can use these along with LVG radiative transfer models to derive physical properties, such as density and temperature of the molecular hydrogen, and the column density of the trace molecule given sufficient transitions.

Since for some molecules studied here collisional rates are not available, we use the Weeds software package⁴ which can perform a simple modeling of the observed spectra, under the assumption of LTE. We use molecular spectroscopy data from the Cologne Database for Molecular Spectroscopy (CDMS) catalog (Müller et al., 2001, 2005) in the calculations.

For ammonia, we used the excitation temperatures derived from the hyperfine structure fits (Sect. 3.2.5 below) while for other molecules we used a value of 8.5 K , as derived from the LVG analysis of the HC_3N and HC_5N data in Cha-MMS1 (Appendix A). We fixed the source sizes for MMS1 and C2 cores

⁴ <https://www.iram.fr/IRAMFR/GILDAS/doc/html/weeds-html/weeds.html>

Table 4. LTE molecular column densities in the Chamaeleon MMS1 and C2 cores compared to TMC-1.

Molecule	$N(\text{MMS1})$ (cm^{-2})	$N(\text{C2})$ (cm^{-2})	$N(\text{TMC-1})$ (cm^{-2})
HC ₃ N	1.7×10^{13}	8.1×10^{12}	2.3×10^{14}
HC ₅ N	3.7×10^{12}	2.2×10^{12}	5.9×10^{13}
HC ₇ N	6.8×10^{11}	3.4×10^{11}	4.6×10^{13}
c-C ₃ H ₂	3.1×10^{13}	1.5×10^{13}	1.9×10^{13}
c-C ₃ HD	6.8×10^{12}	3.7×10^{12}	5.1×10^{12}
CCS	1.4×10^{13}	1.5×10^{13}	1.0×10^{14}
C ₃ S	2.5×10^{12}	2.8×10^{12}	1.4×10^{13}
C ₄ H	1.2×10^{13}	1.1×10^{13}	1.3×10^{14}
¹⁵ NH ₃	5.3×10^{12}	$< 8.0 \times 10^{12}$	
NH ₃	3.7×10^{15}	2.6×10^{15}	5.0×10^{14}
c-C ₆ H ₅ CN	$< 8.9 \times 10^{11}$	$< 6.0 \times 10^{11}$	4×10^{11}

Note: Assumed $T_{\text{ex}} = 8.5$ K for all molecules except of ammonia isotopologues for which $T_{\text{ex}} = 7.6$ K and 5.5 K in Chamaeleon MMS1 and Cha-C2, respectively. TMC-1 values correspond to the cyanopolyne peak (Gratier et al., 2016; McGuire et al., 2018). Ammonia column densities computed using Weeds have been multiplied by 1.038 (see Appendix B) Upper limits are 3σ .

to the mean values derived above. We then adjusted the molecular column density as the only parameter to match the observed line intensities reported in Tables 1 and 2. The resulting column densities are listed in Table 4 along with selected column density ratios in Table 5. For molecules with multiple lines detected, the column densities reported in Table 3 correspond to averages of values derived from individual lines.

In the following subsections we discuss observations of individual molecules detected in the DSS-43 spectra of Chamaeleon MMS1 and C2 and compare their column densities and abundance ratios with reference values for the cyanopolyne peak in TMC-1 from Gratier et al. (2016). In general, column densities of molecular species in the Chamaeleon cores are an order of magnitude lower than in TMC-1, in spite of the higher H₂ column densities (Table 3) compared to 10^{22} cm^{-2} in TMC-1 (Gratier et al., 2016). The high molecular column densities make TMC-1 a preferred target for searches for new molecular species. Notable exceptions are c-C₃H₂ and NH₃, as discussed below.

3.2.1. Cyanopolyynes

A single rotational transition of HC₃N, $J = 2 - 1$, is within the DSS-43 frequency range. The hyperfine splitting is clearly detected in both cores, indicating optically thin emission. LVG models of the DSS-43 and SEST observations are consistent with a kinetic temperature of ~ 8.5 K and a density $\geq 3 \times 10^5 \text{ cm}^{-3}$. Three rotational transitions of HC₅N, from $J = 7 - 6$ to $9 - 8$, are detected in both cores. HC₇N is also detected via stacking analysis (see Sect. 4).

Column densities of cyanopolyynes in the Chamaeleon cores are more than an order of magnitude lower than those in TMC-1 (Gratier et al., 2016). However, the relative abundance ratios HC₃N:HC₅N:HC₇N are similar in both cores, ~ 5 (Table 5). As a reference, the HC₃N:HC₅N abundance ratio in TMC-1 is ~ 4.0 , comparable to the Chamaeleon values, but the HC₅N:HC₇N ratio is lower, ~ 1.3 (Gratier et al., 2016). This dif-

Table 5. Molecular column density ratios in the Chamaeleon MMS1 and C2 cores compared to TMC-1.

Molecules	$R(\text{MMS1})$	$R(\text{C2})$	$R(\text{TMC-1})$
HC ₃ N / HC ₅ N	4.7	3.8	4.0
HC ₇ N / HC ₅ N	0.18	0.16	0.78
C ₄ H / HC ₅ N	3.2	5.0	2.1
CCS / HC ₅ N	4.7	6.9	1.7
CCS / C ₃ S	5.5	5.4	7.4
c-C ₆ H ₅ CN / HC ₅ N	< 0.24	< 0.28	0.09
c-C ₃ H ₂ / HC ₅ N	8.3	7.1	0.32
NH ₃ / HC ₅ N	1000	1200	8.5
NH ₃ / HC ₃ N	210	320	2.1 ^a
NH ₃ / c-C ₃ H ₂	120	170	27
c-C ₃ HD / c-C ₃ H ₂	0.22	0.24	0.28
NH ₃ / ¹⁵ NH ₃	69	> 312	

TMC-1 abundance ratios are from Gratier et al. 2016. ^aPratap et al. (1997) derive independently a factor of 2 higher NH₃/HC₃N abundance ratio of 5.7 at the cyanopolyne peak in TMC-1. When compared with Gratier et al. 2016, their value provides an estimate of the uncertainty of the relative abundance determination.

ference may indicate that the production of long carbon chains is less efficient in Chamaeleon compared to TMC-1.

3.2.2. Polyynes

Three lines of C₄H are detected in both cores. Our column density computations used the latest CDMS value of the dipole moment, 2.1 D, from a quantum chemical calculation by Oyama et al. (2020). For comparison, we use the Gratier et al. (2016) C₄H column density in TMC-1 scaled to a dipole moment of 2.1 D in Tables 4 and 5. The resulting C₄H:HC₅N ratios in the Chamaeleon cores are comparable to that in TMC-1.

3.2.3. Sulfur species

Lines of two sulfur-bearing species, CCS and C₃S are detected in both cores. Compared to TMC-1, the CCS abundance appears slightly enhanced compared to cyanopolyynes, while the CCS/C₃S ratio is similar to that measured in TMC-1.

3.2.4. Cyclopropenylidene isotopologues

Two lines of c-C₃H₂ are detected within the DSS-43 frequency range. The $2_{20} - 2_{11}$ line at 21.6 GHz is seen in absorption against the CMB, as previously observed in TMC-1 (Madden et al., 1989) and consistent with LVG models. The $1_{10} - 1_{01}$ line at 18.3 GHz is seen in emission and was used to derive column density estimates. In contrast to cyanopolyynes, column densities of c-C₃H₂ in the two Chamaeleon cores are comparable to TMC-1. The resulting c-C₃H₂/HC₅N ratio is thus a factor of ~ 25 higher compared to TMC-1 (Table 5).

A line of the deuterated isotopologue c-C₃HD is also detected with a high S/N ratio. The resulting D/H ratio is the same in the two cores, ~ 0.23 , and consistent with the TMC-1 value. Majumdar et al. (2017) carried out a detailed study of c-C₃HD in the solar type protostar IRAS16293-2422 and also derived a high deuterium fraction of 0.14, an order of magnitude higher than the value predicted by their chemical model. A possible ex-

planation is that current astrochemical models appear to over-predict the abundance of $c\text{-C}_3\text{H}_2$ (Agúndez & Wakelam, 2013; Sipilä et al., 2016).

3.2.5. Ammonia isotopologues

The hyperfine structure (HFS) is clearly detected in the (1,1) and (2,2) lines in both sources. HFS fits to the ammonia inversion line spectra, carried out using the IRAM CLASS software (Figure 5), indicate that the NH_3 (1,1) line is optically thick in both Cha-MMS1 and C2 (optical depths of the main hyperfine component equal to 7.6 and 2.9, respectively, Tables 1 and 2). The (2,2) line is optically thin, within the fit uncertainties, and the (3,3) line is only detected in Cha-MMS1. The excitation temperatures within the $K = 1$ rotational ladder can be derived directly from the HFS fits⁵. From the optically thick spectra of the (1,1) inversion transitions, corrected for the source coupling, we derive excitation temperatures of 7.6 and 5.5 K, for Cha-MMS1 and Cha-C2, respectively.

In addition to the excitation temperature, the two K-ladders of ammonia can be used to derive the kinetic temperature. In Appendix B we discuss the derivation of the ammonia rotational temperature, taken as a measure of the kinetic temperature of the gas and the corresponding correction to the molecular column density derived from LTE analysis. We derive kinetic temperatures of 10.9 and 11.1 K in Cha-MMS1 and Cha-C2, respectively.

The ammonia column densities in the two Chamaeleon cores are an order of magnitude higher than in TMC-1. We note that our Cha-MMS1 value of $3.6 \times 10^{15} \text{ cm}^{-2}$ is in good agreement with the value of $1.4 \times 10^{15} \text{ cm}^{-2}$ derived by Tennekes et al. (2006), after correcting for the difference in beam filling factors between DSS-43 and a much larger $80''$ beam of the Parkes telescope. The resulting $\text{NH}_3/\text{HC}_5\text{N}$ abundance ratio is a factor of ~ 125 higher in the Chamaeleon cores compared to TMC-1. The NH_3 abundance enhancement with respect to cyanopolyynes in Chamaeleon compared to TMC-1 is thus a factor of ~ 5 higher compared to that in $c\text{-C}_3\text{H}_2$.

Because of the very high ammonia column density, the (1,1) line of $^{15}\text{NH}_3$ is also detected toward Cha-MMS1 at a S/N ratio of 8. LTE models using Weeds imply a high $^{14}\text{N}/^{15}\text{N}$ isotopic ratio of ~ 690 in ammonia. We note that we assumed the same source size of $52''$ in the computations of the $^{14}\text{NH}_3$ and $^{15}\text{NH}_3$ column densities. Given the high optical depth of the $^{14}\text{NH}_3$ (1,1) line, it is possible that the effective source size is larger compared to $^{15}\text{NH}_3$. A 50% increase in the $^{14}\text{NH}_3$ source size would reduce the column density by a factor of 1.3, bringing the $^{14}\text{N}/^{15}\text{N}$ isotopic ratio in ammonia down to of ~ 525 .

As discussed by Lis et al. (2010), nitrogen displays the largest isotopic variations in the solar system after hydrogen, typically explained by mixing of various proto-solar or pre-solar reservoirs. Earth, Mars, Venus, and most primitive meteorites have nitrogen isotopic ratios within 5% of the terrestrial atmospheric value, $^{14}\text{N}/^{15}\text{N} = 272$ (see Marty et al. (2009)). However, the proto-solar nebula was poorer in ^{15}N , with $^{14}\text{N}/^{15}\text{N} = 450$, as evidenced by infrared and in situ measurements in the Jupiter atmosphere (530^{+380}_{-170} , ISO, Fouchet et al. 2000; 435 ± 57 , Galileo, Owen et al. 2001; 448 ± 62 , from Cassini, Abbas et al. 2004; 450 ± 106 , Cassini, Fouchet et al. 2004) and solar wind measurements (442 ± 131 , 2σ , from Genesis, Marty et al. 2009). The proto-solar $^{14}\text{N}/^{15}\text{N}$ ratio is in agreement with the local interstel-

lar medium (ISM) value (450 ± 22 , Wilson & Rodd 1994; or 414 ± 32 at the birth place of the Sun, Wielen & Wilson 1997).

As discussed by Redaelli et al. (2023) and references therein, nitriles are often enriched in ^{15}N with typical $^{14}\text{N}/^{15}\text{N}$ abundance ratios of 140–460, while N_2H^+ appears instead deficient in ^{15}N with isotopic ratios 580–1000. Using GBT, Lis et al. (2010) measured $^{14}\text{N}/^{15}\text{N}$ ratios of 334 ± 50 and 344 ± 173 (3σ) in ammonia in Barnard 1 and NGC 1333, respectively. In a recent study Redaelli et al. (2023) derived a low isotopic ratio of 210 ± 50 toward NGC 1333 IRAS4A and 390 ± 40 toward the center of L1544.

Redaelli et al. (2023) argue that ammonia ices are enriched in ^{15}N , leading to a decrease in the $^{14}\text{N}/^{15}\text{N}$ ratio when the ices are sublimated back into the gas phase for instance due to the temperature rise in protostellar envelopes. The high $^{14}\text{N}/^{15}\text{N}$ in Cha-MMS1 may suggest that ice sublimation is not a dominant process within the DSS-43 beam.

4. Detections and limits obtained using line stacking analysis

Spectral line stacking of different transitions arising from the same species has been proposed to overcome the low signal-to-noise ratio of these faint signals across wavelength regimes (Chen et al., 2013; Lindroos et al., 2016), and has already shown success in detecting new species at radio frequencies (Loomis et al., 2018; Walsh et al., 2016). By aligning signals from multiple weaker transitions and considering their collective effect, the signal-to-noise ratio can surpass a detection threshold that individual lines might fall below. Loomis et al. (2021) introduced a detection method specialized for sparse data, combining Markov Chain Monte Carlo (MCMC) inference with spectral stacking. Their version of the MCMC code available on GitHub is specific to GBT observations of TMC-1. We generalized this code for use with other sources as described in Appendix C and applied this revised MCMC code to our DSS-43 spectra of HC_7N in the Chamaeleon molecular cloud.

4.1. Longer cyanopolyynes

We detected HC_7N with a high S/N ratio by stacking its rotational transitions from $J = 16 - 15$ to $21 - 20$. Individual spectra are normalized to the brightest line, as predicted by the MCMC model, and weighted by $1/\sigma^2$ in the final average. This approach leads to a robust 9.1σ detection of HC_7N in Cha-MMS1 and a 7.5σ detection in Cha-C2. The resulting spectra are shown in Figs. 3 and 4, lower-right panels and the column densities and abundance ratios are reported in Tables 4 and 5, respectively.

4.2. Upper limit for benzonitrile

The DSS-43 frequency range covers 350 rotational transitions of benzonitrile covering a wide range of line intensities and upper level energies. Figure 6 (upper panel) shows a template LTE model of the benzonitrile emission for a temperature of 8 K, normalized to the intensity of the 18.41 GHz line. Transitions above the green horizontal line, which corresponds to 32% of the intensity of the brightest line, are included in the stacking analysis. This cutoff is arbitrary, but it corresponds to a factor of 10 increase in the integration time to reach the same S/N ratio compared to the brightest line. Including weaker line lines in the analysis does not improve the S/N ratio in the stacked spectrum.

⁵ See Sect. 2.5 of the GILDAS CLASS user manual, <https://www.iram.fr/IRAMFR/GILDAS/doc/pdf/class.pdf>.

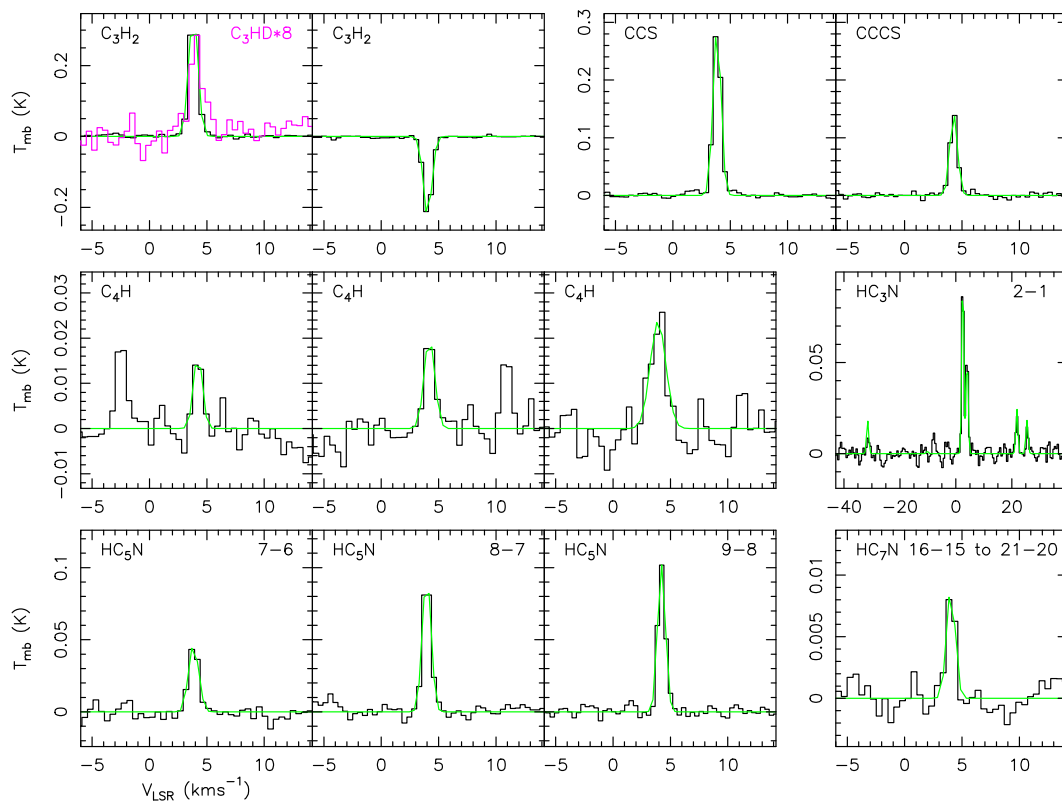


Fig. 4. Spectra of molecular lines other than ammonia detected in Chamaeleon C2 (black and magenta histograms) with fits shown in green.

We extracted spectra of all lines above the cutoff defined above and scaled them to the intensity of the 18.41 GHz line using the LTE template. We then averaged all spectra using $1/\sigma^2$ weighting. The resulting spectra toward Cha-MMS1 and Cha-C2 are shown in Figure 6 (lower panel). No benzonitrile emission is detected in either source. The corresponding 3σ upper limits for the column density are listed in Table 4, and the resulting model spectra are shown as green curves in Figure 6. The 3σ upper limits for the benzonitrile column density achieved in the Chamaeleon sources are a factor of 2 higher than the value derived for TMC-1 (McGuire et al., 2018) and the corresponding upper limits for the relative abundance of benzonitrile with respect to HC_5N are a factor of 3 higher than the TMC-1 value.

4.3. Unidentified features

A single $\sim 7.5\sigma$ unidentified feature is seen in the Cha-C2 spectrum at 22.902 GHz. The feature is not present in the MMS1 spectrum.

5. Discussion

One general result from our study is that column densities of most molecules detected in the Chamaeleon sources are comparatively lower than those in TMC-1. Interestingly, the average temperatures of both Chamaeleon sources are comparable to that of TMC-1, approximately 10 K (an average of the gas and dust temperatures), while the average density of our sources is 10 times or more higher than that of TMC-1.

While the cynaopolyne peak in TMC-1 is a particularly well studied starless core, the presence of molecular abundance gradients across TMC-1 is well established in the literature. Pratap et al. (1997) compare relative abundances of several molecules to-

ward the cynaopolyne, ammonia, and SO peaks in TMC-1. Of particular interest for the results presented here is the $\text{NH}_3/\text{HC}_3\text{N}$ ratio, determined to be 5.8, 16.7, and 25.4 at the three positions, respectively. Hirahara et al. (1992) attribute such variations to differences in the chemical evolutionary stage, with carbon-chain molecules produced in early stages and ammonia in late stages. While the abundance ratios at the ammonia and SO peaks in TMC-1 are higher than that at the cynaopolyne peak, they are still significantly lower than the values derived here for the Chamaeleon cores (Table 5). In the Hirahara et al. (1992) scenario, this would imply that the Chamaeleon cores are characterized by late stage chemistry.

Law et al. (2018) studied carbon chain molecules toward 16 embedded low-mass protostars. The median molecular column densities of HC_3N , HC_5N , CCS, and C_3S in their sample are a factor of 5–12 lower than those in the Cha-MMS1 core, while the C_4H median column density is a factor of 1.4 higher. The resulting median $\text{HC}_3\text{N}/\text{HC}_5\text{N}$ and $\text{CCS}/\text{HC}_5\text{N}$ abundance ratios, ~ 10 , are about a factor 2 higher than the Chamaeleon values, while the $\text{CCS}/\text{C}_3\text{S}$ median abundance ratio, ~ 25 , is a factor of 5 higher. The median $\text{C}_4\text{H}/\text{HC}_5\text{N}$ ratio, ~ 110 , is a factor of 30 higher than the Chamaeleon values (see Table 5 of Law et al. 2018).

Several additional factors may explain the differences in the observed column densities between these sources. First, in higher-density environments such as those in the Chamaeleon sources, molecules likely freeze out onto dust grains more efficiently, as the timescale for the freeze-out is inversely proportional to the gas density (Seo et al., 2019). Second, lower-density regions like TMC-1 may have longer chemical timescales, allowing molecular species to persist for extended periods and resulting in higher gas-phase column densities (Majumdar et al., 2015). Third, lower-density cores may allow greater pene-

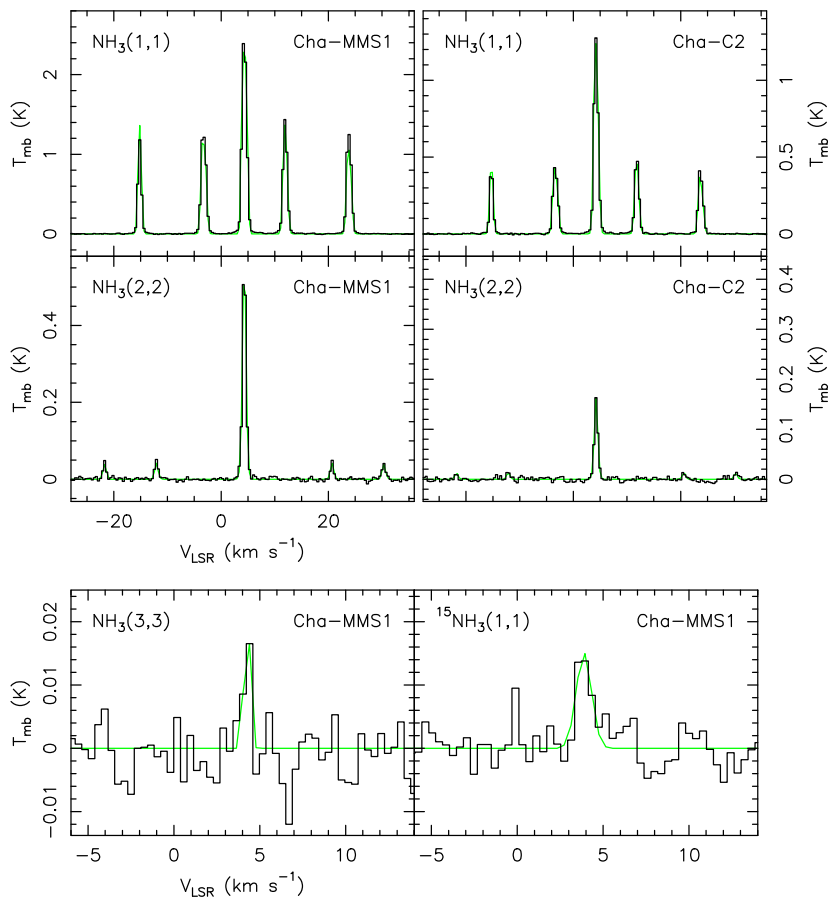


Fig. 5. Spectra of the detected ammonia inversion lines in Chamaeleon MMS1 and C2. The transition and source are labeled in each panel. The observational data are shown as black histograms, and spectral fits are shown in green.

tration of ambient UV photons, facilitating photodesorption of molecules from grain surfaces and leading to higher abundances (Öberg et al., 2007). Fourth, variations in cosmic-ray ionization rates between these sources could significantly influence gas-phase chemistry, contributing to the differences in the observed column densities (Taniguchi et al., 2024). (Seo et al., 2019). It is also possible that these cores have different ages, as well as different initial elemental abundances, leading to different C/O ratios compared to TMC-1, is also a major possibility (Taniguchi et al., 2024). For example, Loison et al. (2014) reported that several carbon-chain groups (such as C_n , C_nH , C_nH_2 , $C_{2n+1}O$, C_nN , $HC_{2n+1}N$, $C_{2n}H^-$, and C_3N^-) show a strong dependence on the assumed C/O ratios and evolutionary stage. In particular, for carbon chains gas-phase chemistry dominates in the early stages (10^5 years), whereas depletion becomes significant in the later stages.

Determining which of these processes dominates in our case will require future studies employing advanced chemical models, including isotope chemistry observed in our samples. This will be a focus of a future investigation.

6. Summary

Here we have extended the survey for organics in the southern hemisphere to 1.3 cm by observing two cores in the Chamaeleon

complex using NASA’s Deep Space Network antenna in Canberra, Australia, over the frequency range of 18 to 25 GHz. We surveyed the class 0 protostar Cha-MMS1 and the prestellar core Cha-C2, which represent two stages in the evolution of dense cores. We used the detections of ammonia, cyanopolyynes, and far-infrared dust continuum to characterize the density and temperature in the Chamaeleon cores and calculate the molecular column densities and their relative ratios.

The main results can be summarized as follows:

- Several molecules are detected in both cores including HC_3N , HC_5N , C_4H , CCS , C_3S , NH_3 , and $c-C_3H_2$. A longer cyanopolyne, HC_7N , is detected with high confidence via spectral stacking analysis.
- While molecular column densities in the two Chamaeleon cores are typically an order of magnitude lower compared to the cyanopolyne peak in TMC-1, the molecular abundance ratios are in general agreement with the TMC-1 values. The two exceptions are $c-C_3H_2$, which is enhanced by a factor of ~ 25 with respect to cyanopolyynes in the Chamaeleon cores, and ammonia, which is enhanced by a factor of ~ 125 .
- A deuterated isotopologue $c-C_3HD$ is detected in both cores, with a high D/H ratio of ~ 0.23 in $c-C_3H_2$, in general agreement with observations of other sources, such as TMC-1 or IRAS1629-2422.

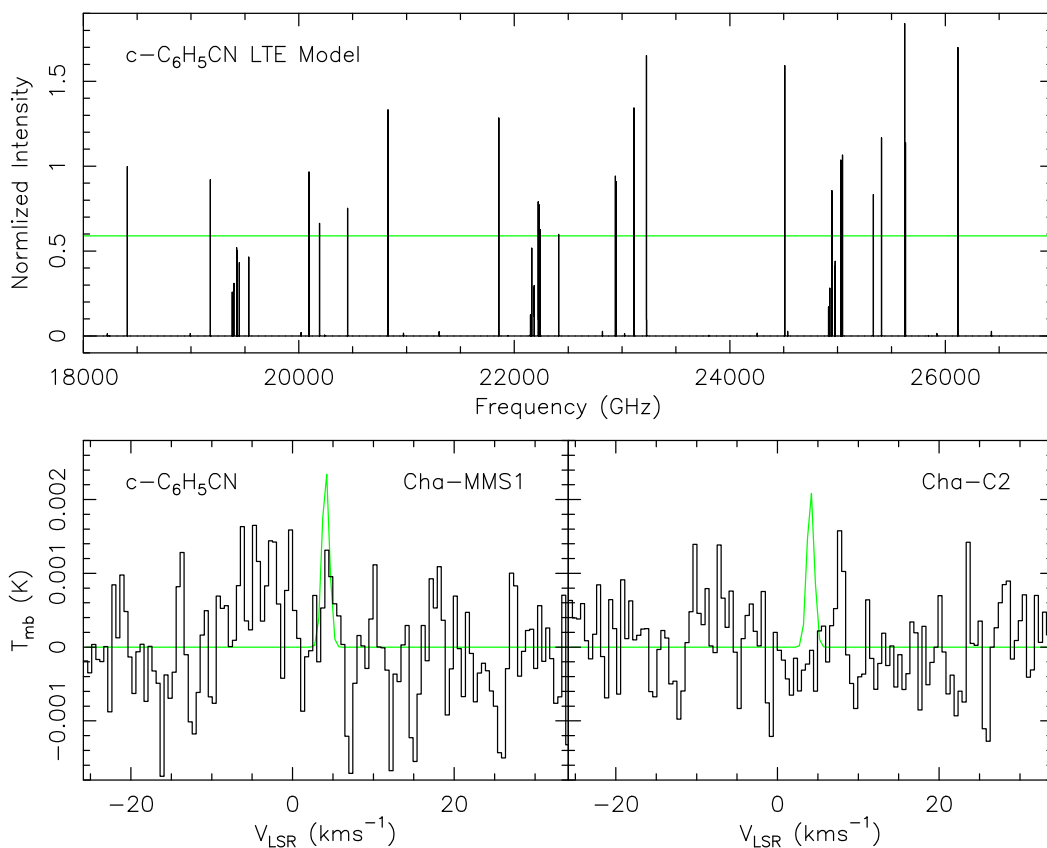


Fig. 6. (Upper) LTE model spectrum of benzonitrile in the DSS-43 frequency range for a temperature of 8.5 K. Line intensities are normalized to the 18.41 GHz transitions. Transitions above the green horizontal lines are included in the stacking analysis. (Lower) Stacked spectra of benzonitrile toward Cha-MMS1 and Cha-C2 normalized to the 18.41 GHz line. Green curves are 3σ upper limits LTE models corresponding to column densities reported in Table 4.

- A rare isotopologue of ammonia, $^{15}\text{NH}_3$, is also detected in Cha-MMS1 suggesting a high $^{14}\text{N}/^{15}\text{N}$ ratio of ~ 690 in ammonia. However, this ratio may be artificially enhanced due to the high optical depth of the $^{14}\text{NH}_3$ (1,1) line, which increases the effective source size.
- The ring molecule benzonitrile, a tracer for the non-polar molecule benzene, is not detected in either Chamaeleon core. The 3σ upper limits for the benzonitrile column density achieved are about a factor of 2 higher than the TMC-1 value (McGuire et al., 2018) and the resulting upper limits for the relative abundance of benzonitrile with respect to HC_5N are a factor of 3 higher than that measured in TMC-1.

Our results suggest that the chemical composition of the two Chamaeleon cores is different in several aspects from that of TMC-1. However, the chemical composition of the observed organics in the two Chamaeleon cores are similar to each other despite representing different stages of core evolution. This result suggests there may be a steady state solution during this period and it will require comparison to earlier and later stages of cores to reveal the relationship between chemical composition and age. Ongoing DSS-43 observations of additional sources will determine whether these conclusions are generally applicable to other southern star forming cores.

Acknowledgements. This research was carried out at the Jet Propulsion Laboratory, California Institute of Technology, under a contract with the National Aeronautics and Space Administration (80NM0018D0004) and funded through the internal Research and Technology Development program. We thank Steve Lichten, Joe Lazio, and the DSN staff for their support and assistance with the

DSS-43 observations, and an anonymous referee for helpful comments. L.M. acknowledges financial support provided by DAE and the DST-SERB research grant (MTR/2021/000864) from the Government of India.

References

- Abbas, M. M., et al. 2004, *ApJ*, 602, 1063
- Agúndez, M., & Wakelam, V., 2013, *Chemical Reviews*, 113, 8710
- Belloche, A., Schuller, F., Parise, B., et al. 2011, *A&A* 527, A145
- Bop, C., & Lique, F. 2025, *A&A*, in press
- Burkhardt, A. M., Loomis, R. A., Shingledecker, C. N., et al. 2021, *Nature Astronomy*, 5, 181
- Cernicharo, J., Agúndez, M., Cabezas, C., et al. 2021, *A&A*, 649, L15
- Cernicharo, J., Cabezas, C., Fuentetaja, R., et al. 2024, *A&A*, 690, L13
- Chen, C.-T., et al. 2013, *ApJ*, 773, 3
- Corby, J. F., Jones, P. A., Cunningham, M. R., et al. 2015, *MNRAS*, 452, 3969
- Cordiner, M. A., Charnley, S. B., Wiström, E. S., et al. 2012, *ApJ*, 744, 131
- Cummins, S.E., Linke, R.A., & Thaddeus, P. 1986, *ApJ*, 60, 819
- Dickens, J. E., Langer, W. D., and Velusamy, T., 2001, *ApJ*, 558, 693
- Faure, A., Lique, F., & Wiesenfeld, L. 2016, *MNRAS*, 460, 2103

- Forman-Mackey, D., Hogg, D. W., Lang, D., et al. 2013, *PASP*, 125, 306
- Fouchet, T., et al. 2000, *Icarus*, 143, 223
- Fouchet, T., et al. 2004, *Icarus*, 172, 50
- Frerking, M. A., Langer, W. D., & Wilson, R. W. 1979, *ApJ*, 262, 590
- Galli, P.A.B., Buoy, H., Olivares, J., et al., 2021, *A&A*, 646, 46
- Goldsmith, P.F., Bergin, E.A., & Lis, D.C. 1997, *ApJ*, 491, 615
- Goldsmith, P.F., & Langer, W.D. 1999, *ApJ*, 517, 209
- Gratier, P., Majumdar, L., Ohishi, M., et al. 2016, *ApJS*, 225, 25
- Hanni, N., et al. 2022, *Nature*, Comm., 13, 3639
- Hildebrand, R.H. 1983, *QJRAS*, 24 267
- Hirahara, Y., Suzuki, H., Yamamoto, S., et al. 1992, *ApJ*, 394, 539
- Kitadai, N. & Maruyama, S. 2018, *Geosci. Front.*, 9, 1117
- Kontinen, S., et al. 2000, *A&A*, 361, 704
- Kuiper, T. B. H., Franco, M., Smith, S., et al. 2018, *J. Astronomical Instrumentation*, 8, 1950014
- Kuiper, T. B. H., Langer, W. D., and Velusamy, T., 1996, *ApJ*, 468, 761
- Langer, W. D., Velusamy, T., Kuiper, T. B. H., et al., 1995, *ApJ*, 453, 293
- Langer, W. D., Velusamy, T., Kuiper, T. B. H., et al., 1997, *ApJL*, 480, L63
- Langer, W. D., Kuiper, T. B. H., and Velusamy, T. 1998, *Astro. Lett. and Communications*, 37, 59
- Law, C.J., Öberg, K.I., Bergner, J.B., & Graninger, D., 2018, *ApJ*, 863, 88
- Lefloch, B., Bachiller, R., Ceccarelli, C., et al. 2018, *MNRAS*, 477, 4792
- Lindroos, L., et al. 2016, *MNRAS*, 462, 1192
- Lipkus, A.H., Yuan, Q., Lucas, K.A., et al. 2008, *J. Org. Chem.* 73, 4443
- Lis, D.C., & Goldsmith, P.F. 1990, *ApJ*, 356, 195
- Lis, D.C., Seraby E., Keene, J.B., et al. 1998, *ApJ*, 509, 299
- Lis, D.C., Roueff, E., Gerin, M., et al. 2002, *ApJ*, 571, L55
- Lis, D.C., Wootteen, A., Gerin, M., et al. 2010, *ApJ*, 710, L49
- Loison, J.-C., Wakelam, V., Hickson, K.M., et al. 2014, *MNRAS*, 437, 930
- Loomis, R.A., et al. 2018, *ApJ*, 155, 182
- Loomis, R.A., et al. 2021, *Nature Ast.*, 5, 188
- Madden, S.C., Irvine, W.M., Matthews, H.E., et al. 1989, *ApJ*, 97, 1403
- Majumdar, L., Gorai, P., Das, A., & Chakrabarti, S.K. 2015, *ApSS*, 360,64
- Majumdar, L., Gratier, P., Andron, I., et al. 2017, *MNRAS*, 467, 3525
- Marty, B., et al. 2009, *Geochim. Cosmochim. Acta*, 74, 340
- McClure, M.K., et al. 2023, *Nature Ast.*, 7, 431
- McGuire, B. A., Burkhardt, A. M., Kalenskii, S., et al. 2018, *Science*, 359, 202
- McGuire, B. A., Loomis, R. A., Burkhardt, A. M., et al. 2021, *Science*, 371, 1265
- McGuire, B. A., 2022, *ApJS*, 259, 30
- Müller, H., Schlöder, F., Stutzki, J., & Winnewisser, G. 404 2005, *Journal of Molecular Structure*, 742, 215
- Müller, H., Thorwirth, S., Roth, D. A., & Winnewisser, G. 406 2001, *A&A*, 370, L49
- Öberg, K.I., Fuchs, G.W., Awad, Z., et al. 2007, *ApJ*, 662, L23
- Owen, T., Mahaffy, P. R., Niemann, et al. 2001, *ApJ*, 553, L77
- Oyama, T. Ozaki, H. Sumiyoshi, Y., et al. 2020, *ApJ*, 890, 39
- Peng, R., Langer, W. D., Velusamy, T., Kuiper, T. B. H., and Levin, S., 1998, *ApJ*, 497, 842
- Pineda, J.L., et al. 2019, *ApJ*, 866,1
- Powner, M. W., Gerland, B., & Sutherland, J. D. 2009, *Nature*, 459, 239
- Pratap, P., Dickents, J.E., Snell, R.L., et al. 1997, *ApJ*, 486, 862
- Redaelli, E., Bizzocchi, L., Caselli, P., et al. 2023, *A&A*, 674, L8
- Rocha, W. R. M., McClure, W. L., Sturm, J. A., et al., 2024, *A&A*, 693, A288
- Rivilla, V. M., Colzi, L., Jiménez-Serra, I., et al. 2022, *ApJ*, 929, L11
- Ruddigkeit, L., van Deursen, R., Blum, L. C. & Reymond, J.-L. 2012, *J. Chem. Inf. Model.*, 52, 2864
- Seo, Y., Majumdar, L., Goldsmith, P.F., et al. 2019, *ApJ*, 871, 134
- Sipilä, Spezzano, S., & Caselli P., 2016, *A&A*, 591, L1
- Sturm, J.A., et al. 2024, *A&A*, 679, 138
- Taniguchi, K., Gorai, P., & Tan, J.C. 2024, *ApSS*, 369, 34
- Tennekes, P.P., et al. 2006, *A&A*, 456, 1037
- Tsilali, A.E., Belloche, A., Commerçon, B., & Menten, K.M. 2013, *A&A* 557, A98
- van der Tak, F.F.S., Black, J.H., Schöier, F.L., et al. 2007, *A&A* 468, 627
- Velusamy, T., Kuiper, T. B. H., and Langer, W. D. 1995, *ApJL*, 451, L75
- Virkler, K., Kocz, J., Soriano, M., et al., 2020, *ApJ Suppl.*, 251, 1
- Walsh, C., et al. 2016, *ApJ*, 823, L10
- Wakelam, V., Loison, J.-C., Herbst, E., et al. 2015, *ApJS*, 217, 20
- Wenzel, G., Cooke, I.R., Changala, P.Bryan. et al. 2024, *Science*, 386, 810
- Widicus Weaver, S.L., et al. 2017, *ApJS*, 232, 3
- Wielen, R., & Wilson, T. L. 1997, *A&A*, 326, 139
- Wilson, T. L., & Rood, R. T. 1994, *ARA&A*, 32, 191

Appendix A: LVG analysis of HC₃N and HC₅N

We use a large velocity gradient (LVG) model of HC₃N and HC₅N spectra to determine the best fit densities and temperatures for the cores where organic molecules are detected. For both species theoretical calculations exist for the collisional rate coefficients and there are sufficient number of spectral lines detected from different transitions to constrain the solutions. We use the offline version of the RADEX code (van der Tak et al., 2007) to calculate intensities I (K km s⁻¹), opacity τ , and level population as a function of density, kinetic temperature, and column density. We consider a range of T_k , $n(\text{H}_2)$, and column density $N(\text{HC}_n\text{N})$ suggested by earlier observations of the Chamaeleon cores to find a good fit to the data. We use the line widths listed in Table 1 and a background temperature $T_{bg} = 2.73\text{K}$. For HC₃N we use collisional rate coefficients from Faure et al. (2016) which are available from the Leiden Atomic and Molecular database⁶ while those for HC₅N are from Bop & Lique (2025). Given the low gas temperatures, in both cases we assume that hydrogen is para-H₂. The resulting intensities were compared to the DSN and SEST data for HC₃N. The DSN and SEST beam widths are similar, $\sim 45''$ and $55''$, respectively and comparable to the size of the cores, as discussed in Section 2. We exclude the 7 mm Mopra observations of HC₃N and HC₅N (Cordiner et al., 2012) because its beam size, $96''$ to $77''$, is much larger than those of the DSN and SEST, and larger than the source size. These differences in angular resolution introduces uncertain filling factor corrections for beam dilution and beam coupling.

Figure A.1 shows results for HC₃N intensities for densities, $n(\text{H}_2) = 3 \times 10^4, 3 \times 10^5, \text{ and } 3 \times 10^6 \text{ cm}^{-3}$ which cover the range of densities derived from dust emission and C¹⁸O, as discussed in Sect. 3.1. We also consider four values of kinetic temperatures, as follows: $T_k = 7.1 \text{ K}$ is the LTE value derived by Cordiner et al. (2012) for HC₃N and HC₅N, 8.5 K is our best solution for HC₃N and HC₅N, 10.9 K is derived from our ammonia data, and 16 K was chosen to study the impact of a higher temperature on the distribution of intensities. The solution for each T_k is shown in a separate panel and the DSN observed intensity is plotted as a circle and the SEST ones as squares. The best fit solution is for $T_k = 8.5 \text{ K}$ and column density $N(\text{HC}_3\text{N}) = 8.4 \times 10^{13} \text{ cm}^{-2}$. There is little difference between the solutions at densities 3×10^5 and $3 \times 10^6 \text{ cm}^{-3}$. At densities above $3 \times 10^5 \text{ cm}^{-3}$ the transitions considered here are approaching thermalization. In fact, low-frequency HC₅N lines are fully thermalized at densities as low as 10^5 cm^{-3} , as suggested by their critical densities. In the LVG solution all the observed HC₃N lines have an opacity $\tau < 0.2$ and the excitation temperatures range from 7.4 K to 8.6 K consistent with the lines approaching thermal equilibrium for the case $T_k = 8.5 \text{ K}$. We note that a solution with a low density of $3 \times 10^4 \text{ cm}^{-3}$ and a higher temperature of 16 K is also consistent with the observations. However, these temperature and density values are inconsistent with other the values suggested by other tracers (Sect. 3.1).

For HC₅N we ran an LVG analysis over the same range of T_k and $n(\text{H}_2)$ and the results are shown in Figure A.2. The column density $N(\text{HC}_5\text{N}) = 1.75 \times 10^{12} \text{ cm}^{-2}$ for the best fit temperature $T_k = 8.5 \text{ K}$, and is very similar for the other three values of T_k . The intensities of the three lines detected with the DSN are shown as red circles. The constraints on physical parameters from HC₅N is less stringent than for HC₃N as SEST did not detect any HC₅N lines. We have excluded the HC₅N data from Mopra (Cordiner et al., 2012) for the same reasons discussed above for HC₃N. Without enough contrast in excitation conditions we

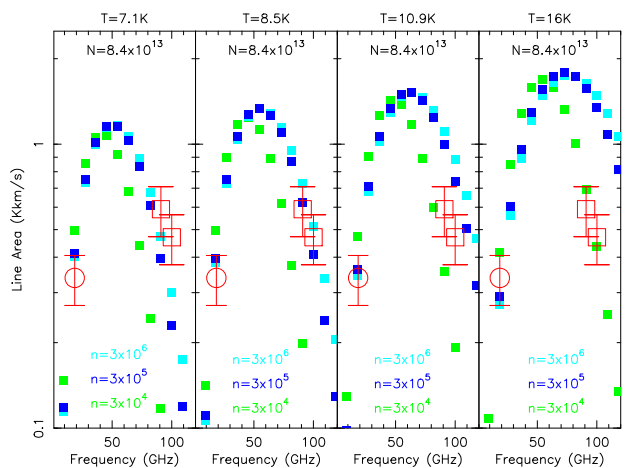


Fig. A.1. LVG models of the HC₃N emission in Cha-MMS1 for different densities (filled cyan, blue, and green squares, as labeled). The four panels correspond to kinetic temperatures of 7.1, 8.5, 10.9, and 16 K, left to right, respectively. The open red circle shows our DSN observation while the red squares are SEST observations of Kontinen et al. (2000). The error bars correspond to a typical 20% absolute calibration uncertainty.

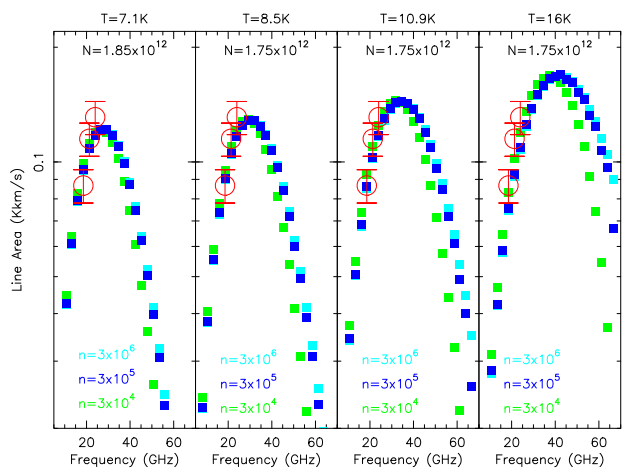


Fig. A.2. LVG models of the HC₃N emission in Cha-MMS1 for different densities (filled cyan, blue, and green squares, as labeled). The four panels correspond to kinetic temperatures of 7.1, 8.5, 10.9, and 16 K, left to right, respectively. The open red circles show our DSN observations. The error bars correspond to a typical 10% relative calibration uncertainty.

can only constrain T_k from 8.5 K to 16K, and $n(\text{H}_2)$ to be greater than $3 \times 10^4 \text{ cm}^{-3}$. However, the column density is insensitive over the likely range of temperatures and densities considered here, as well as those indicated by the HC₃N analysis, and that is the key parameter needed for interpreting chemical abundances.

Appendix B: Ammonia rotational temperatures and column densities

In the case of ammonia, the column density calculation is complicated by the presence of two different temperatures describing the rotational level population: the excitation temperature T_{ex} within a given K -ladder, and the rotational temperature T_{rot} describing the relative populations of the metastable rotational levels at the bottom of each K -ladder. In the absence of allowed

⁶ <https://home.strw.leidenuniv.nl/moldata/>

radiative transitions between different K -ladders, the latter can be taken as a measure of the gas kinetic temperature.

In spite of this complication, we can use the excitation temperature derived from the HFS fit to determine the ammonia column densities in the lowest metastable level of each K -ladder. These values can then be used to determine the rotational (kinetic) temperature of the gas.

The upper level molecular column density of a rotational transitions within the telescope beam can be computed from the observed integrated line intensity of the transitions using the standard formula (see, e.g., Lis et al. 2002)

$$N_u = \frac{8\pi k\nu^2}{hc^3 A_{ul}} \frac{1}{1 - [J_\nu(T_{bg})/J_\nu(T_{ex})]} \int T_R dv, \quad (\text{B.1})$$

where ν is the line frequency, T_{ex} is the excitation temperature, A_{ul} is the Einstein spontaneous emission coefficient, E_u is the upper level energy, $J_\nu(T) = hv/k/(e^{hv/kT} - 1)$ is the radiation temperature of a blackbody at a temperature T , T_{bg} is the cosmic background temperature (2.7 K), and $\int T_R dv$ is the opacity and beam efficiency corrected integrated line intensity.

The ratio of the populations of the upper and lower levels of the inversion transitions at the bottom of each K -ladder is given by $N_l/N_u = g_l/g_u \exp((E_u - E_l)/kT_{ex})$. Therefore, the population in the lowest metastable level of each K -ladder can be computed as

$$N_l = \frac{g_l}{g_u} e^{(E_u - E_l)/kT_{ex}} \frac{8\pi k\nu^2}{hc^3 A_{ul}} \frac{1}{1 - [J_\nu(T_{bg})/J_\nu(T_{ex})]} \int T_R dv. \quad (\text{B.2})$$

Here, the excitation temperature is that derived from the HFS fit and the resulting column densities for Cha-MMS1 and Cha-C2 are listed in Table B.1.

The rotational temperature can then be computed from the populations of two metastable levels at the bottom of different K -ladders, denoted i and j , using the formula

$$N_i/N_j = \frac{g_i}{g_j} \exp\left(-\frac{E_i - E_j}{kT_{rot}}\right). \quad (\text{B.3})$$

From the lower-level column densities of the (1,1) and (2,2) transitions reported in Table B.1 we derive rotational temperatures of 10.9 K both in Cha-MMS1 and Cha-C2.

The total NH_3 column densities computed by the Weeds package use the partition functions computed assuming that all levels are populated at the assumed excitation temperature, T_{ex} . However, the rotational levels of ammonia are populated according to two temperatures: the excitation describing the population within a given K -ladder and the rotational temperature connecting the different K -ladders. To first approximation, in the low temperature limit applicable to the Chamaeleon sources, the correction factor to the partition function can be computed including only the $K = 1$ and 2 ladders,

$$Q(T_{ex}, T_{rot}) = Q(T_{ex}) C(T_{rot}) = Q(T_{ex}) \left(1 + \frac{g_2}{g_1} \exp\left(-\frac{E_2 - E_1}{kT_{rot}}\right)\right), \quad (\text{B.4})$$

where the $Q(T_{ex})$ is the standard partition function from the spectroscopic catalog and indices 1 and 2 refer to the lowest energy metastable levels in the $K = 1$ and 2 ladders, respectively. For $T_{rot} = 11$ K, the correction factor $C = 1.038$, suggesting that most of the population is within the $K = 1$ ladder. The population in the ground state of the $K = 3$ ladder is less than 0.1% of that in the ground state of the $K = 1$ ladder. For consistency with

Table B.1. Ammonia column densities in the Chamaeleon cores.

Transition	$N_l(\text{MMS1})$	$N_l(\text{C2})$
	(cm^{-2})	(cm^{-2})
NH_3 (1,1)	1.41×10^{14}	5.43×10^{13}
NH_3 (2,2)	5.39×10^{12}	2.08×10^{12}
NH_3 (3,3)	7.41×10^{10}	–

Note: Calculations assume $T_{ex}=7.6$ K and 5.5 K for Cha-MMS1 and Cha-C2, respectively, as derived from the HFS fit to the NH_3 (1,1) lines.

other molecules, the total NH_3 column densities reported in Table 4 are computed from opacity corrected line intensities of the (1,1) line using the Weeds package, and applying the correction factor C , derived above.

Appendix C: Line stacking analysis

We adapted the TMC-1 Markov Chain Monte Carlo fitting and LTE spectral simulator scripts of Loomis et al. (2021), refactoring the codebase and improving user accessibility. Originally tailored for Green Bank Telescope (GBT) observations of TMC-1, the code has been restructured to support a range of customizable user inputs, making it adaptable to new sources. It has also been supplemented with documentation. A user-friendly logging system with real-time progress tracking and upgraded file management was introduced to handle various MCMC runs and automate all statistical preprocessing. Walkers have been reconfigured to consistently initialize within physical bounds, reducing the need for manual fine-tuning between molecular species. To address the degeneracy between source size and column density, users may fix the source size if it can be determined externally, thereby tightening constraints on column density, or leave it free if unknown. Column density may also be initialized via maximum likelihood estimation to further stabilize the inference process. The result is a robust open-source software tool for MCMC inference of spectra, successfully validated on the GOTHAM dataset, and publicly available on GitHub⁷.

To apply the Python-based MCMC tool to the DSN dataset, HC_5N was selected as a benchmark molecule due to the presence of multiple spectral lines within the DSS-43 frequency range. This choice was strategic for several reasons: 1) the MCMC algorithm fits all emission lines simultaneously, diverging from traditional single-line methods; 2) each line possesses a high signal-to-noise ratio; 3) as HC_5N is a member of the cyanopolyne family, accurate parameter estimation for this molecule provides informed initial guesses for parameter space exploration of structurally related, larger molecules like HC_7N or HC_9N .

The MCMC workflow begins with data reduction and preparation, following the methodology of the GOTHAM survey analysis (Loomis et al., 2021). We performed an initial spectral simulation across the entire DSN bandwidth using the LTE spectral simulator configured with DSS-43 telescope properties. For each transition exceeding a threshold intensity, a spectral window of $4.1 \pm 1.5 \text{ km s}^{-1}$ was defined and a local noise level was calculated in the vicinity of the line.

Following spectral reduction, we applied a Python-based MCMC script to derive posterior distributions and covariances

⁷ <https://github.com/KahaanGandhi/Chamaeleon-MCMC>

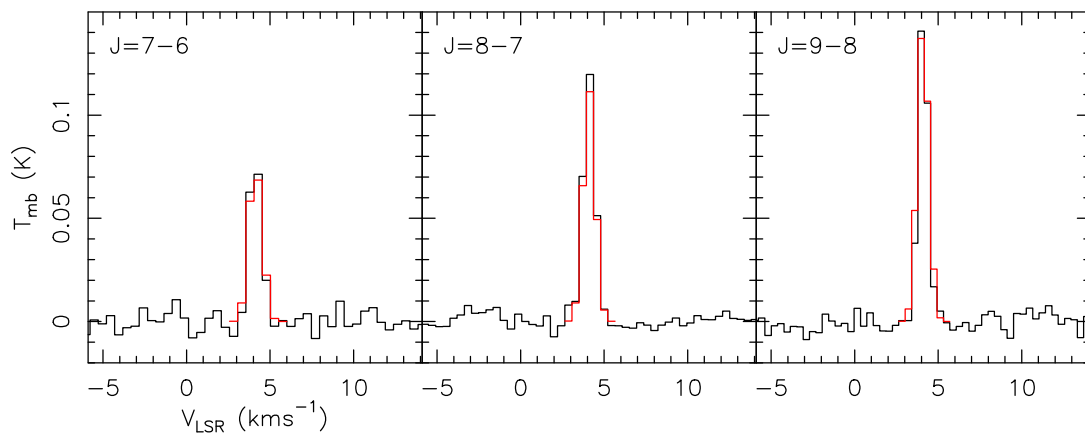


Fig. B.1. Observed spectra of the J=7–6 to 9–8 lines of HC₅N in Cha-MMS1 (black histograms) compared to model spectra generated using best-fit values from the Python MCMC fit (red histograms).

for the five free parameters: source size, column density (N_c), excitation temperature (T_{ex}), source velocity (V_{LSR}), and line width (ΔV). We implemented the affine-invariant ensemble sampler provided by the emcee toolkit (Foreman-Mackey et al. 2013), exploring the parameter space with 128 walkers for 10,000 steps. Non-informative priors were used to maintain physically plausible best-fit values. The log-likelihood function was defined as the negative half of the sum of squared residuals between observed and modeled spectra, weighted by the inverse variance.

For HC₅N in both MMS1 and C2 cores, we begin with a “template run” — initializing walkers in a wider range using no prior information or assumptions to prioritize a thorough exploration of the parameter space. After assessing the quality of these fits visually through corner plots and ensuring that the parameter distributions align with our physical expectations, the posteriors from these template runs are used as priors for subsequent analyses of HC₅N and HC₇N, and can also be extended to larger cyanopolyynes. The best-fit values align with previous surveys, successfully benchmarking the MCMC algorithm and providing confidence for future applications. The 50th percentile parameter values for Cha-MMS1 are overlaid with the reduced DSN spectra in Figure B.1.

Having verified that the MCMC approach successfully derives parameter values in agreement with previous higher-frequency surveys of Chamaeleon (Cordiner et al., 2012), we applied it to the detection of HC₇N. This longer cyanopolyne presents 8 emission lines in the DSS-43 frequency range, with 7 falling within the region relatively free of excess noise. The posteriors from the HC₅N template run serve as the priors for the HC₇N analysis. The resulting corner plot for HC₇N in Cha-MMS1 is shown in Fig. C.1, with similar posterior distributions for most parameters compared to HC₅N, and a column density an order of magnitude lower, consistent with those discussed in Sect. 5.

For this detection, we also employ spectral line stacking to further boost the signal-to-noise ratio. This technique aligns multiple transitions along the velocity axis, enhancing the overall signal by averaging across several lines. In our analysis, we stack the rotational transitions from $J = 16 - 15$ to $23 - 22$, normalizing individual spectra to the brightest line and weighting by $1/\sigma^2$ for the final average, as shown in Fig. 4. This approach leads to a robust 9.1σ detection of HC₇N in Cha-MMS1 and a 7.5σ detection in Cha-C2 (Fig. 3 and 4, lower-right panels). The

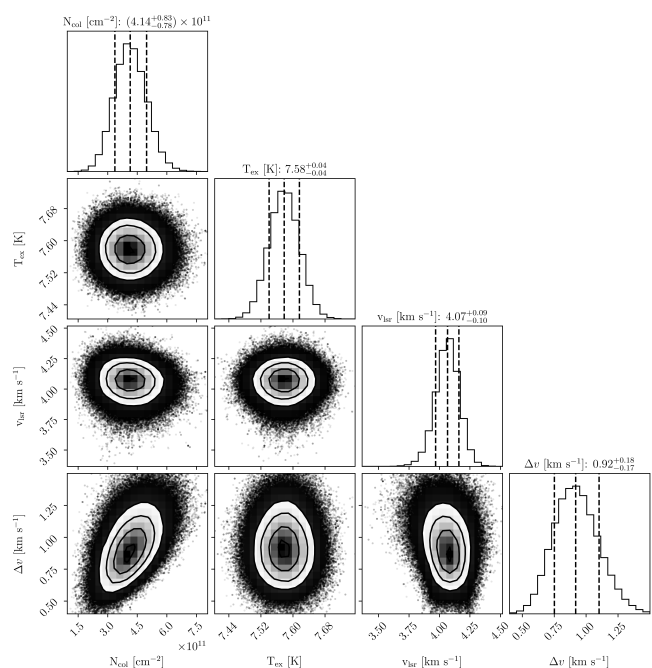


Fig. C.1. Corner plot for the MCMC fit of HC₇N parameter covariances and distributions in the Cha-MMS1. The diagonal shows the probability distributions of each parameter as histograms, with vertical lines marking the 16th, 50th, and 84th percentiles, corresponding to $\pm 1\sigma$ for a Gaussian posterior. The off-diagonal scatter plots depict the correlations between pairs of parameters, with each axis representing one of the fitted parameters. The beam-averaged best-fit column density is consistent with the Weeds pencil beam value listed in Table 4.

MCMC method shows great promise for detecting other heavy molecules.